J Mater Sci (2019) 54:5570–5583

Computation and theory

Atomistic simulations of grain boundary energies in austenitic steel

Sutatch Ratanaphan[1,*], Rajchawit Sarochawikasit[2], Noppadol Kumanuvong[1], Sho Hayakawa[3], Hossein Beladi[4], Gregory S. Rohrer[5], and Taira Okita[6]

[1] Department of Tool and Materials Engineering, King Mongkut's University of Technology Thonburi, 126 Pracha Uthit Rd, Thung Khru, Bangkok 10140, Thailand
[2] Department of Computer Engineering, King Mongkut's University of Technology Thonburi, 126 Pracha Uthit Rd, Thung Khru, Bangkok 10140, Thailand
[3] School of Engineering, The University of Tokyo, Tokyo, Japan
[4] Institute for Frontier Materials, Deakin University, Geelong, VIC 3216, Australia
[5] Department of Materials Science and Engineering, Carnegie Mellon University, Pittsburgh, PA 15213-3890, USA
[6] Research into Artifacts, Center for Engineering, The University of Tokyo, Kashiwa, Japan

Received: 27 August 2018
Accepted: 27 December 2018
Published online: 7 January 2019

ABSTRACT

The energies of 388 grain boundaries with a range of misorientations and grain boundary plane orientations have been calculated using the meta-atom embedded atom method potential recently developed to simulate an austenitic twinning-induced plasticity (TWIP) steel. A comparison between the simulated grain boundary energies and the measured grain boundary population in an austenitic TWIP steel revealed that at fixed misorientations, there is a strong inverse correlation between the energy and the population. In addition, the Bulatov–Reed–Kumar five-parameter grain boundary energy function for face-centered cubic metals was used to produce a larger, more nearly continuous set of grain boundary energies. Interestingly, these interpolated grain boundary energies were consistent with the simulated energies and also inversely correlated with the measured grain boundary populations in an austenitic TWIP steel.

Introduction

Iron-based face-centered cubic (fcc) alloys, known as austenitic steels, have been used in a wide range of applications due to their high strength, formability, and corrosion resistance [1–5]. It was found that the lowest energy grain boundary (the coherent twin boundary) can effectively prevent inter-granular corrosion in 304, 316, and 316L austenitic steels [5–7], as well as radiation-induced segregation and irradiation-assisted stress corrosion cracking in 316L stainless steels [3, 8]. In addition, the deformation twin boundaries that develop during strain-

Address correspondence to E-mail: sutatch.ratanaphan@mail.kmutt.ac.th

https://doi.org/10.1007/s10853-018-03297-4

hardening can also block the movement of dislocations, leading to a desirable combination of high strength and ductility [1, 2, 9, 10]. Twinning-induced plasticity (TWIP) in high-manganese austenitic steels is the focus of an increased number of studies because of the application of these steels for automotive parts that require high formability as well as high energy absorption [1, 2, 9, 10].

Grain boundary crystallographic space, described by using five-macroscopic degrees of freedom (three for the lattice misorientation and two more for the grain boundary plane orientation), is large (there are $\sim 6 \times 10^3$ distinguishable grain boundaries if the space is discretized in 10° increments) [11]. Nonetheless, it is now possible to examine the relative areas of different grain boundaries and grain boundary population distributions in austenitic steels [12–19]. A recent three-dimensional electron backscatter diffraction (3D-EBSD) study of an austenitic TWIP steel demonstrated that the grain boundary population and energy distributions were, on average, inversely correlated [12]. In other words, the grain boundaries with higher energies make up a smaller fraction of the population than those with lower energies. Nonetheless, the range of energy anisotropy reported in [12] was different from a previous measurement performed on a 304 austenitic stainless steel [20]. Specifically, the ratio between the coherent twin boundary energy and the average grain boundary energy (0.73) obtained from the 3D-EBSD measurement [12] is significantly larger than the one (0.01) measured using a zero creep method [20]. The discrete characteristics of the energy reconstruction method lead to an underestimation of the depth of cusps where the energies change rapidly with misorientation angle [11, 21]. This is why the twin boundary to average boundary energy ratio in the reconstructed grain boundary energy distribution is so much larger than value recovered from the zero creep measurements [12, 20].

Previously, grain boundary energy distributions in fcc metals (Al, Au, Cu, and Ni) have been calculated using the embedded atom method (EAM) [22, 23]. Interestingly, the simulated grain boundary energies were consistent with the reconstructed energy distribution derived from the 3D-EBSD measurements, at least for the grain boundaries that made up the largest fraction of the observations [24, 25]. Therefore, atomistic simulations provide a reliable method to explore grain boundary energy distributions (GBEDs). There are no prior reports of atomistic simulations of grain boundary energies in austenitic TWIP steels. The energies of symmetric grain boundaries in pure γ-Fe [26] have been calculated in the past using a Finnis–Sinclair (FS) potential [27]. In that study, the boundary energy of the Σ3 coherent twin boundary terminated on (111) planes, calculated at 800 K, contributed to a large energy cusp and the ratio between the coherent twin boundary energy and the average grain boundary energy was 0.02; this is comparable to the result that was determined by the zero creep energy measurement (0.01) [20].

It is not known how closely the energies of γ-Fe correspond to those of a high-manganese TWIP steel. Considering the differences in the moduli (the moduli of γ-Fe are C_{11} = 243 GPa, C_{12} = 138 GPa, and C_{44} = 122 GPa [26] while the moduli of the TWIP steel are C_{11} = 175 GPa, C_{12} = 83 GPa, and C_{44} = 97 GPa [28]), one might suppose that the grain boundary energies will not be the same. To calculate grain boundary energies for the high-manganese TWIP steel, an embedded atom method (EAM) potential developed for the alloy is required. Until recently, no appropriate potentials were available. One of the challenges of simulating a complex alloy is to accurately depict the complicated arrangement of alloying components in the minimum energy grain boundary state. A simplified solution to this problem was recently proposed by Wang et al. [28], who developed a meta-atom EAM potential for an austenitic TWIP steel. This meta-atom EAM potential was developed so that simulations of identical meta-atoms in the fcc structure reproduce known properties of the alloy such as the lattice constant, cohesive energy, stacking fault energy, vacancy formation energy, and elastic moduli [28–31], eliminating the need to track each type of element and their different interactions. While this is a significant approximation, it should be noted that studies of one austenitic steel found that the distribution of the alloying elements at grain boundaries was relatively homogenous and independent of the grain boundary misorientation and grain boundary plane orientation [8]. This meta-atom embedded atom method (EAM) potential has been used to investigate dislocation slip and deformation twinning in an austenitic TWIP steel [28] and might also be used to calculate grain boundary energies in the same steel.

The main purpose of the present study is to calculate the energies of 388 grain boundaries by using

the meta-atom EAM potential for an austenitic steel (Fe–22Mn–0.6C) [28]. The energies are also extrapolated throughout the five-parameter space using the Bulatov–Reed–Kumar (BRK) function for fcc metals [32]. These energies are then compared to experimentally observed grain boundary population and energy distributions in a similar austenitic steel (Fe–18Mn–0.6C–1.5Al) and some high-purity fcc metals [24, 25]. If the grain boundary energy distribution in this complex alloy is similar to other fcc metals, this might simplify the problem of specifying grain boundary energies for other alloys.

Method

The atomistic models of grain boundaries were constructed as bicrystals in a periodic box of size $15a_0/2$, where a_0 is the lattice parameter. There were 388 distinct grain boundaries with grain boundary misorientations ranging from Σ3 to Σ385. The computational scheme used in the present study was similar to the previous simulations of grain boundary energies in fcc metals [22, 23] and body-centered cubic (bcc) metals [33, 34]. The meta-atom EAM potential for Fe–22Mn–0.6C austenitic TWIP steel used in this study was developed by Wang et al. [28]. It should be noted that the stacking fault energy obtained from this EAM potential (19 m Jm^{-2}) is comparable with the Fe–18Mn–0.6C–1.5Al austenitic TWIP steel (~ 25 m Jm^{-2}) that was used for the experimental measurements of the grain boundary population and energy distributions [12, 35]. The conjugate-gradient method in the Large-scale Atomic/Molecular Massively Parallel Simulator (LAMMPS) code [36] was used to find minimum energy structures and energies of grain boundaries at 0 K. The grain boundary energy for each macroscopic grain boundary was obtained from the lowest energy of 100 to 10000 energy minimized initial configurations [23, 33, 34].

The Bulatov–Reed–Kumar (BRK) function for grain boundary energy in fcc metals contains 43 numerical parameters obtained by fitting with simulated grain boundary energies for Al, Au, Cu, and Ni to smooth curves [32]. A scaffolding of lower-dimensional subsets of the three grain misorientation parameters and the two boundary plane orientation parameters was used in the fitting processes [32]. The random boundary energy (E_{RGB}), an independent parameter for each element, determines the overall energy scaling. Apart from the energy scaling (E_{RGB}), there are 42 dimensionless parameters that describe the grain boundary energy anisotropy. While 27 parameters are held constant, the other 15 parameters are linearly scaled with an element-dependent shape factor (Φ). The shape factor for TWIP austenitic steel (Φ_{TWIP}) is obtained from a hypothetical relationship plotted as a function of the ratio between stacking fault energy (SFE) and E_{RGB} (Fig. 1). Because the ratio of the SFE (0.019 Jm^{-2}) and E_{RGB} (the highest grain boundary energies = 1.516 Jm^{-2}) in the TWIP steel (0.01) is lower than the one in Cu (0.04), the value of Φ_{TWIP} (1.17) is slightly greater than Φ_{Cu} (1.0). Based on this scheme, this energy function requires only two parameters: the lowest (the coherent twin boundary) and the highest grain boundary energies (the random boundary energy, E_{RGB}) to fully describe energy for a given grain boundary, [32].

Results

The grain boundary energies of the austenitic TWIP steel are tabulated with their macroscopic parameters in the Online Supplemental Material. A comparison between previously reported grain boundary energies in (fcc) γ-Fe [26] and our simulated energies of the same boundaries in the austenitic steel is shown in Fig. 2. Although there is some scatter, grain boundary energies in γ-Fe and the austenitic steel are strongly correlated (correlation coefficient = 0.9). The similarity of meta-atom embedded atom method (EAM) potential for austenitic steel [28] and the potential for γ-Fe [27] may contribute to this correlation. The different temperatures used in the calculations (0 K for the alloy and 800 K for pure Fe) may contribute to the difference. However, the grain boundary energies in the pure material would be expected to decrease at higher temperature [37, 38], so this does not explain the difference. It should also be noted that grain boundary energies in pure γ-Fe were obtained from a single initial configuration [26], but grain boundary energies in the present work were obtained by considering multiple initial configurations. Crystallographically identical grain boundaries with different initial atomic configurations have different minimum grain boundary energies. To increase the chance of finding the global minimum boundary energy, many different initial

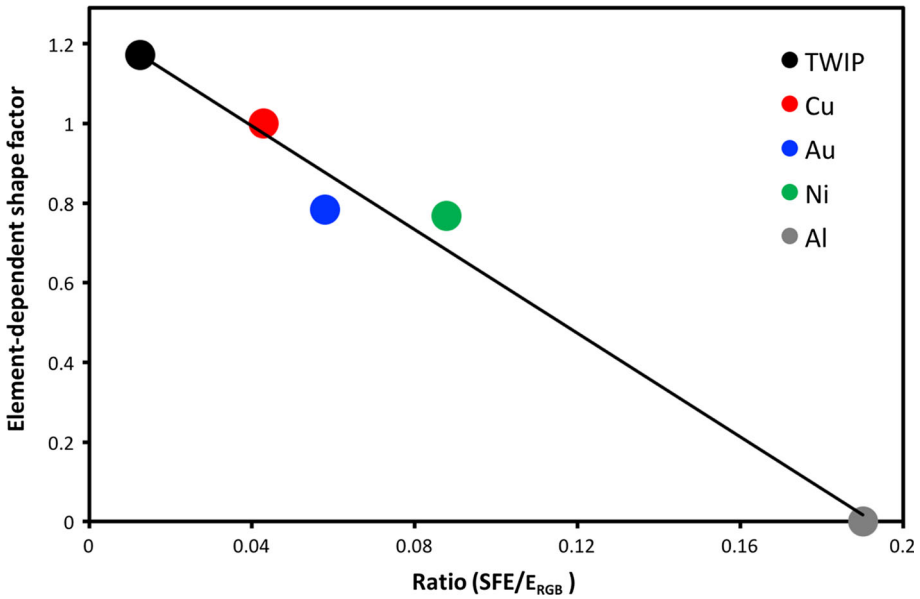

Figure 1 The relationship between element-dependent shape factors and the ratios between stacking fault energies (SFE) and energies of random boundaries (E_{RGB}) in Cu (red), Au (blue), Ni (green), and Al (gray) [32]. Note that the shape factor for austenitic TWIP steel (black) is derived from the inverse relationship.

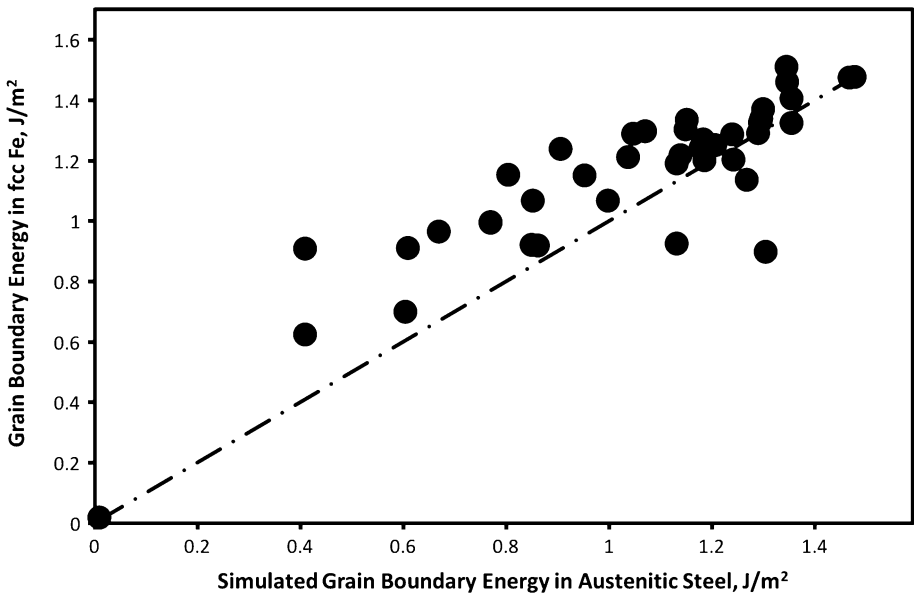

Figure 2 A comparison between simulated grain boundary energies in the austenitic TWIP steel and previously simulated grain boundary energies in pure γ-Fe [26]. A dashed line represents a perfect fit (a unit slope).

configurations should be sampled [23]. Therefore, grain boundary energies in pure γ-Fe [26] are likely to be higher than the energies of the same boundaries in the austenitic TWIP steel.

The simulated grain boundary energies are compared to the measured grain boundary energy and population distributions for the Σ3 and Σ9 misorientations (see Fig. 3). The positions of tilt, twist, symmetric (180°-twist), and improper quasi-symmetric (180°-tilt) grain boundaries are generated in GBToolbox [39, 40] (see Fig. 3a, e). The distribution of measured grain boundary energies at the Σ3 misorientation in Fig. 3b [12] is comparable to the simulated grain boundary energy in Fig. 3c. While the minimum energies in both distributions are found at the (111) twist position (the coherent twin boundary), the high-energy boundaries obtained from the measurement and atomistic simulation are not the same. Specifically, high calculated grain boundary energies are aligned along with the great circle perpendicular to the (111) orientation and maxima are reached at {110} orientations (see Fig. 3c), whereas high boundary energies in the measured grain boundary energy distribution (Fig. 3b) do not exhibit clear maxima. The energy anisotropy characterized by the energy ratio between the minimum boundary energy

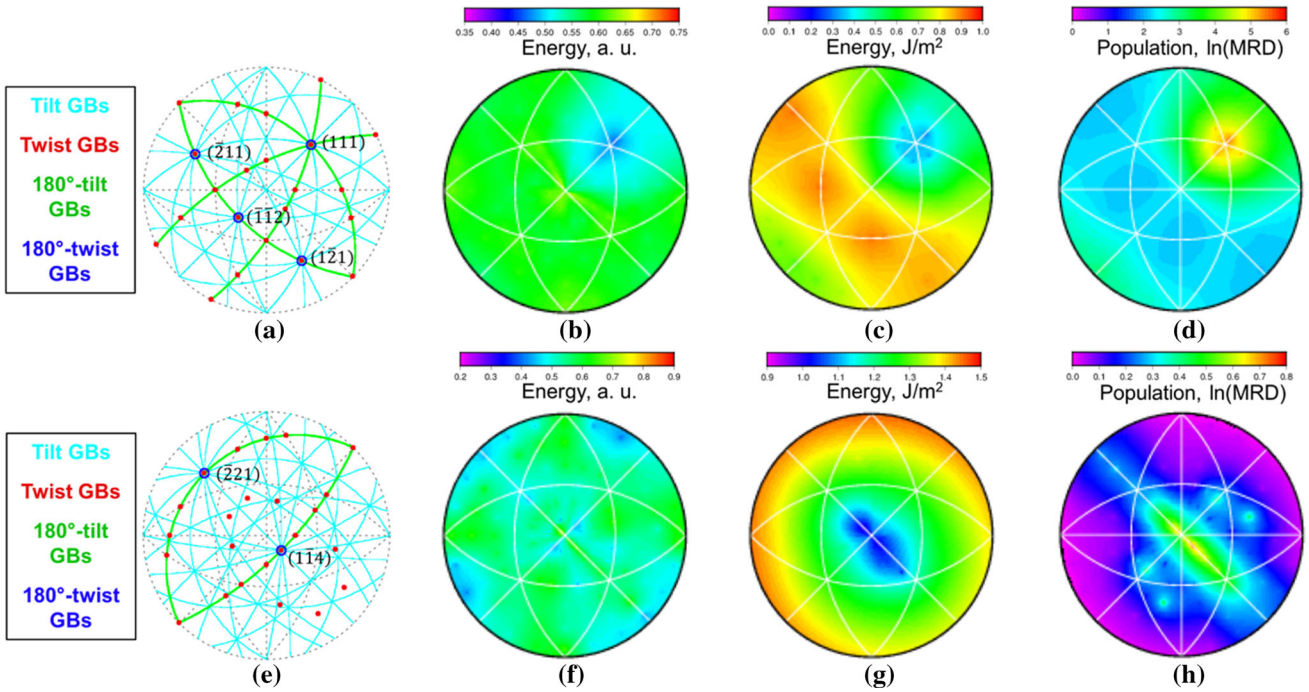

Figure 3 Schematic representation of grain boundaries at Σ3, 60°/[111] (**a**) and Σ9, 39°/[110] (**e**), produced in GBToolbox [39, 40]. The distributions of measured grain boundary energies, simulated grain boundary energies, and relative grain boundary areas for Σ3 (**b**–**d**) and Σ9 (**f**–**h**) misorientations. For the plots of simulated grain boundary energies, 41 and 23 distinct data points are used at the Σ3 and Σ9 misorientations, respectively. It should also be noted that the symmetry increases the numbers of data points. The distributions are plotted on a stereographic projection using the bicrystal reference frame with the [001] and [100] directions normal to the page and horizontal to the right within the page, respectively. The measured grain boundary population and energy were obtained from Ref. [12]. The relative grain boundary areas are plotted in units of multiples of a random distribution (MRD).

(coherent twin boundary) and the average grain boundary energy for the current results is 0.01, consistent with the energy ratio between the coherent twin energy and the average grain boundary energy in the 304 austenitic steel measured using the zero creep method [20]. Figure 3d shows the measured grain boundary population at the Σ3 misorientation derived from the 3D-EBSD measurements [12]. The population maximum at the coherent twin boundary corresponds to the minima in the measured and simulated grain boundary energy distributions in Fig. 3b, c, respectively. This is consistent with the well-known inverse correlation between grain boundary energy and population for fcc metals [24, 25, 41].

The distributions of measured and simulated grain boundary energies at the Σ9 misorientation are shown in Fig. 3f, g, respectively. While the measured grain boundary energy distribution indicates that the energy of the $(\bar{2}21)$ symmetric tilt boundaries (0.266 a.u.) is much smaller than the energy of the $(1\bar{1}4)$ symmetric tilt boundaries (0.893 a.u.), our simulated results suggest that the energy of the $(\bar{2}21)$ symmetric tilt boundaries (1.148 Jm^{-2}) is greater than the energy of the $(1\bar{1}4)$ symmetric tilt boundaries (0.803 Jm^{-2}). While the simulated energies do not agree well with the measurements, they do agree with the relative areas (Fig. 3h) [24, 25]. We observe that the $(1\bar{1}4)$ symmetric tilt boundaries, which is the lowest simulated energy at the Σ9 misorientation, is the most frequently observed boundary at the Σ9 misorientation as shown in Fig. 3h. The relative area measurement, which is a direct measurement, is more robust than the grain boundary energy, which is interpreted from triple junction geometries [24, 25], so the inverse correlation between the simulated grain boundary energy distributions (GBEDs) in Fig. 3c, g and the grain boundary character distribution (GBCD) at the Σ3 and Σ9 misorientation shown in Fig. 3d, h, respectively, supports the validity of the calculated energies.

When all 388 boundaries are considered with equal weighting, there is no significant correlation between the experimental and simulated grain boundary energies. However, by using weighted least squares method [42], a linear fit weighted by grain boundary population (see red line in Fig. 4) shows a strong correlation coefficient (0.7). The improvement in the correlation when the most frequently observed boundaries are given more weight agrees with the idea that the experimental assessment of the grain boundary energy is more reliable when it is based on more observations [24, 25]. The boundary with the highest population (502 MRD) is the coherent twin boundary, which corresponds to the measured (simulated) grain boundary energy of 0.401 a.u. (0.019 Jm^{-2}). It is also observed that low-energy boundaries in the simulated data set are more frequently observed than the high-energy boundaries. While the experimental energy of the coherent twin boundary is relatively low, it is much larger than the energy of the Σ55 (311) symmetric grain boundary, which is the lowest measured boundary energy (0.164 a.u.). However, because the population of the Σ55 (311) symmetric grain boundary is relatively small (0.4 MRD), we surmise that there was an insufficient number of observations to determine a reliable energy [24]. For such cases, it is better to use the inverse correlation between the grain boundary population and the grain boundary energy [12, 24, 25, 43–48] to validate the grain boundary energy distribution.

Figure 5 shows the relationship between the measured grain boundary population and the boundary energies obtained from atomistic simulations. The simulated energies are strongly correlated with the grain boundary population ($R = -0.8$). The outliers are the Σ37 (111) twist boundary and the Σ33 (554) symmetric tilt boundary, marked with black and orange solid circles, respectively. These boundaries have a higher population because of their proximity ($\sim 10°$) to the coherent twin boundary [49]; the discretization of the data and the non-uniform shapes of the discrete bins broadens the maxima around the most populated grain boundary types and artificially increases the population of nearby boundaries. It should be noted that the inverse correlation between population and energy in the austenitic steel has different slopes at each misorientation, consistent with the previous investigations for fcc metals [24, 25, 41].

Figure 6 shows a comparison between the simulated and interpolated grain boundary energies in the

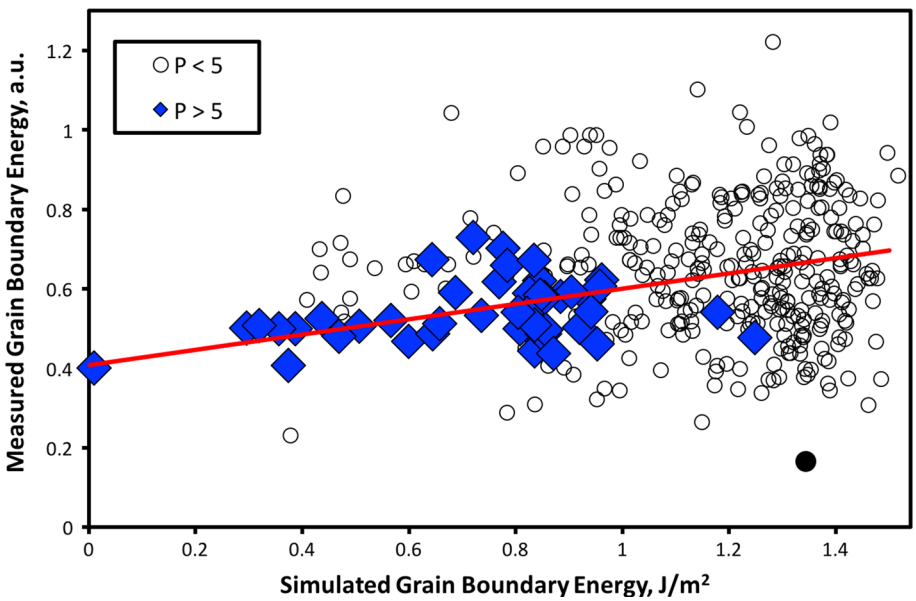

Figure 4 The relationship between experimentally derived and simulated grain boundary energies. The horizontal axis denotes the simulated grain boundary energies, while the vertical axis denotes the experimental grain boundary energies [12]. A weighted linear fit for the energies of boundaries with a population (P): $P > 5$ MRD (blue diamonds) is shown by a red line. Grain boundaries with population of $P < 5$ MRD are marked with circles and the Σ55 (311) symmetric grain boundary (the lowest measured grain boundary energy) is marked with a solid black circle.

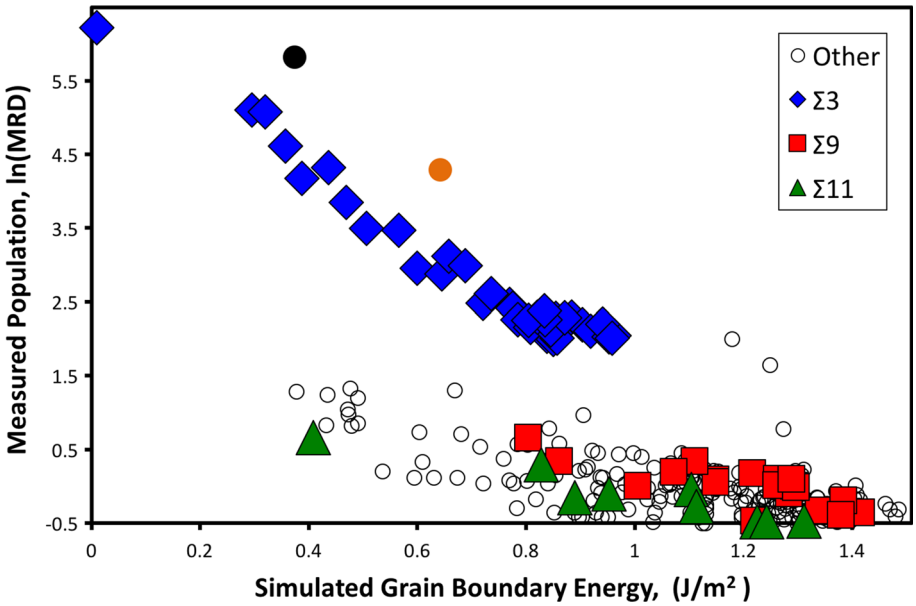

Figure 5 The relationship between the simulated grain boundary energies and the measured population in the austenitic TWIP steel [12]. The data are assigned into four distinct groups: Σ3 (blue diamonds), Σ9 (red squares), Σ11 (green triangles), and others (circles). The Σ37 (111) twist boundary and the Σ33 (554) symmetric tilt boundary are marked with black and orange solid circles, respectively.

austenitic steel using the BRK function for fcc metals [32]. There is scatter in the data, which deviates from the perfect fit represented as a dashed line in the plot. Specifically in the low-energy boundary region, the energies of <111> twist boundaries obtained from the grain boundary energy function [32] are lower than the trend line. Furthermore, at the high-energy boundary region, the interpolated energies of {10 6 2}{10 6 2}, {4 2 0}{4 2 0}, and {11 7 2}{11 7 2} boundaries are larger than the simulated boundary energies. The scatter between the interpolated and simulated grain boundary energies implies that the two alloy-specific parameters (the lowest and highest grain boundary energies) used in the interpolated function do not perfectly describe the energy anisotropy in the austenitic steel, but they certainly produce a reasonable

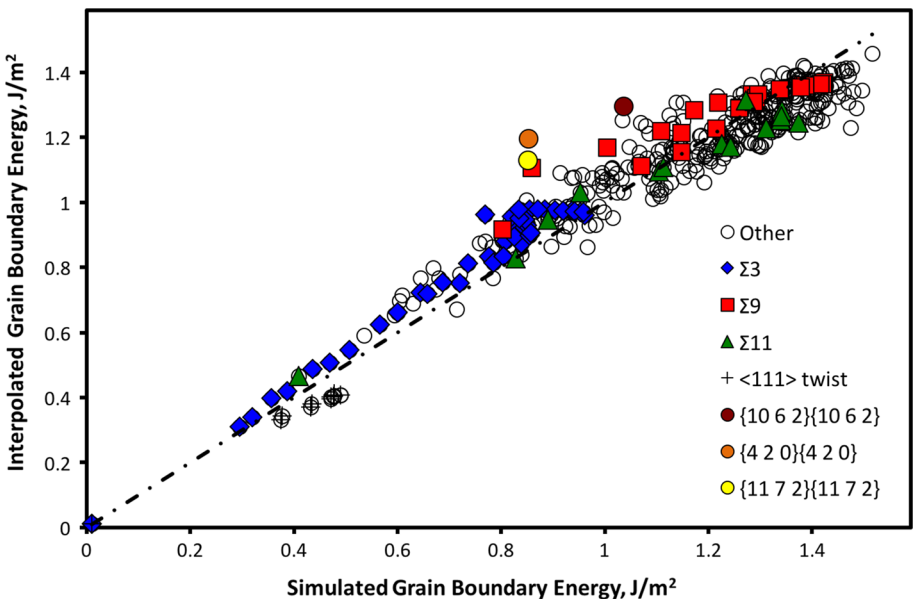

Figure 6 The relationship between the simulated energies of grain boundaries in austenitic steel and the energies of the same boundaries derived from the BRK grain boundary energy function for fcc metals [32]. These 388 grain boundaries are assigned into five distinct groups: Σ3 (blue diamond), Σ9 (red square), Σ11 (green triangle), others (circle), and <111> twist boundaries. Circles with brown, orange, and yellow colors are {10 6 2}{10 6 2}, {4 2 0}{4 2 0}, and {11 7 2}{11 7 2} boundaries, respectively. A dashed line represents a perfect fit (a unit slope).

estimate for the majority of boundaries. It should be noted that the grain boundary energy function [32] was created to model results from Al, Au, Cu, and Ni [22]. The present study uses an EAM potential with a lower stacking fault energy (SFE = 19 m Jm^{-2}) than Al, Au, Cu, and Ni, and this may be one reason for the differences [22]. Nonetheless, the plot in Fig. 6 reveals a strong correlation between the simulated and interpolated grain boundary energies with a correlation coefficient of 0.96. Therefore, the BRK boundary energy function for fcc structured metals can be used to interpolate arbitrary grain boundary energies in the austenitic steel.

Discussion

In this study, grain boundary energies in an austenitic TWIP steel were calculated from an atomistic simulation by using the meta-atom potential developed by Wang et al. [28]. When the components of an alloy strongly segregate to grain boundaries, they can have a profound effect on the grain boundary structures and energies through adsorptions [50, 51]. If the inhomogeneity of the solute distribution becomes critical and results in significant grain boundary segregation and embrittlement [52], the meta-atom EAM potential and the BRK grain boundary energy function cannot be used in grain boundary energy calculations. However, in an austenitic stainless steel (316L), it has been observed that the solute is distributed homogeneously with respect to grain boundary type [8]. While radiation-induced segregation [3, 8] in the same material is strongly dependent on the grain boundary misorientation and plane, that would not be a factor in the material investigated in this work. Also, a recent atom probe tomography (APT) study of the distribution of elements at a grain boundary in a single phase fcc high-entropy alloy ($Fe_{40}Mn_{40}Co_{10}Cr_{10}$) revealed no segregation or ordering [53]. Assuming that solute is also distributed homogeneously in the TWIP steel considered here, it is reasonable to model it with the meta-atom EAM potential, where it behaves as an fcc structured metal with modified interactions between the atoms. While the effects of segregation and ordering on the grain boundary energy in this steel are not known, previous calculations suggest they are relatively small and that they will not critically impact the findings. Changes in the atomic structure of grain boundaries in Cu, and of the arrangement of segregated Ag, change the grain boundary energy by 3% or less [54]. Furthermore, grain boundaries in Cu with segregated Ag transform between two ordered states, one with a monolayer of Ag and one with a bilayer of silver, but the energies of these states differ by only 0.1 mJm^{-2}, an amount much smaller than the expected accuracy of these calculations [55]. If similar effects occur in the TWIP steel considered here, similar errors are expected. It should be noted that we are also assuming that the results calculated from the potential fabricated for the Fe–22Mn–0.6C TWIP steel can be compared to the experimental observations from the Fe–18Mn–0.6C–1.5Al TWIP steel without significant errors. The broad agreement between the calculated results and the experimental observations suggests that the composition difference causes inconsistencies in the energy that are similar to or smaller than the experimental uncertainties.

These simulated grain boundary energies were compared with experimentally determined grain boundary energy and area distributions obtained from 3D-EBSD measurements [12]. We found that the simulated and measured boundary energies in austenitic steel were correlated only for the most frequently observed grain boundaries (Fig. 4), which was consistent with the previous study comparing simulated and measured grain boundary energies in nickel [24]. One of the most interesting results was the strong inverse relationship between the simulated energies and the measured grain boundary population in the austenitic TWIP steel. The inverse correlation has a different slope at each misorientation (Fig. 5). While the grain size could affect the grain boundary population in fcc structured metals and alloys in some cases [18, 56, 57], simulations have shown that the GBCD reaches steady state after reasonable grain growth has occurred [47] and the observed inverse relationship is similar to ones obtained from high-purity nickel [24] and copper [41]. Therefore, the inverse relationship between the population and energy for polycrystals evolving by grain growth has been established for many materials [11] and in particular for fcc materials [12, 24, 25, 43]. Observing this inverse correlation between the simulated grain boundary energies and the measured relative grain boundary areas provides evidence for the validity of the simulated energies. It is also observed in Fig. 6 that the simulated energies were strongly correlated with the interpolated energies

obtained from the BRK function [32] using only two parameters (the lowest and the highest grain boundary energies). Assuming the meta-atom EAM method accounts for solute effects, it appears that the energies of grain boundaries in a complex alloy exhibit the same trends as pure metals with the same structure. This is demonstrated by Fig. 7, which shows that simulated grain boundary energies in the austenitic steel and nickel [22] are strongly correlated with a correlation coefficient of 0.99. However, it should be noted that if the components of the alloy strongly segregated in a non-homogeneous way, we would not expect this strong correlation. Interestingly, it is also observed that grain boundary energies in Ni and austenitic steel that are lower than 1 Jm^{-2} are linearly scaled with the ratio of a_0C_{44}, the scaling factor previously identified for pure fcc metals [22]. Nonetheless, for the higher energy grain boundaries, the energies in Ni are distinctly lower than the ones projected from the scaling ratio of a_0C_{44}. Because the stacking fault energies in the austenitic steel (SFE = 19 m Jm^{-2}) and nickel (SFE = 127 m Jm^{-2}) are significantly different, this might cause the deviation. Note that similar deviations from the scaling are found when gold (SFE = 31 m Jm^{-2}) and copper (SFE = 44 m Jm^{-2}), which also have relatively lower stacking fault energies, are compared to nickel [22].

Figure 8 shows comparisons between simulated and interpolated energies of twist and symmetric tilt boundaries. For <100> tilt, 100> twist, <110> twist, and <111> tilt boundaries, the simulated energies are comparable with the ones derived from the BRK function [32]. However, the simulated and interpolated energies are significantly different for <110> tilt, and <111> twist boundaries. For <110> tilt boundaries, the interpolated energies for the maxima located at rotational angles of 27°, 81°, and 148° are greater than the simulated ones. The interpolated energies of these three maxima are scaled with the parameters that are held constant. Therefore, the significant differences between the interpolated and simulated boundary energies for <110> tilt grain boundaries might be corrected by modifying the fixed parameters in the BRK function. It should be also noted that the energy maximum for the <111> twist boundaries obtained by using the BRK function [32], which are lower than the simulated grain boundary energies (see Figs. 6, 8), is scaled with Φ_{TWIP}. This suggests that using a different shape factor for the austenitic TWIP steel might improve the agreement. Because the energies of <111> twist boundaries are scaled with the ratio of a_0C_{44} (see Fig. 7), this parameter might offer a better scaling factor. However, considering the overall strong correlation between the simulated and interpolated grain boundary energies, we did not explore modifications to the various fitting parameters. The overall agreement indicates that the BRK grain boundary energy function is a reliable approach for producing nearly continuous sets of boundary energies in TWIP steels and other fcc structured metals with very little input data.

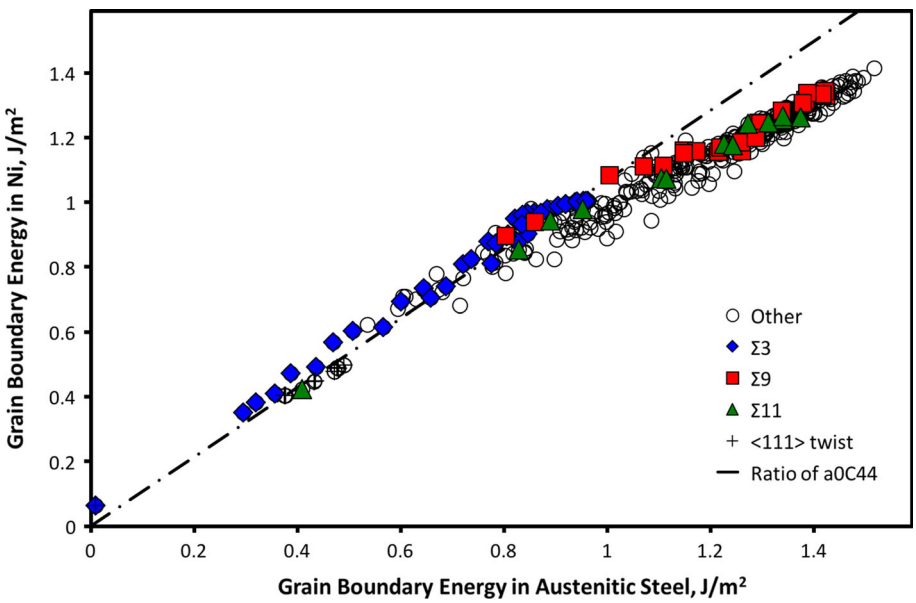

Figure 7 The relationship between the simulated energies of grain boundaries in austenitic steel and the energies of the same boundaries in Ni [22]. The dashed line represents the scaling ratio of a_0C_{44} = 1.07.

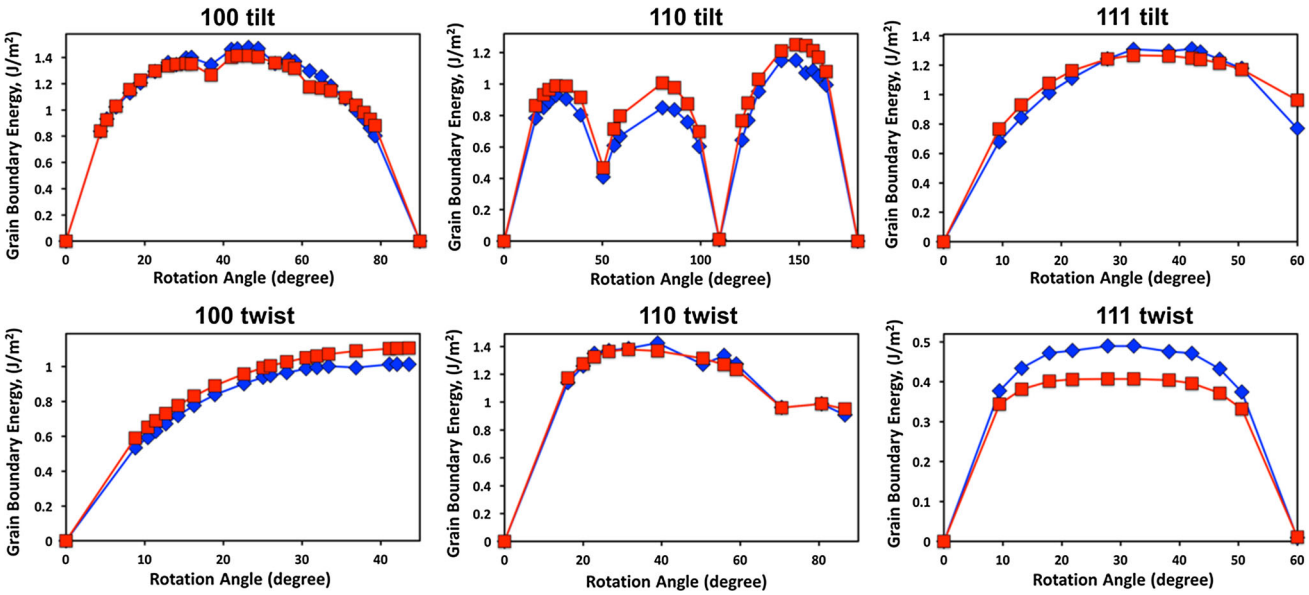

Figure 8 Comparisons of the simulated energies (blue diamonds) and the energies (red squares) obtained from the grain boundary energy function [32]. The energies of <100>, <110>, and <111> tilt/twist grain boundary energies in the austenitic steel are plotted as a function of rotation angle (°).

The BRK grain boundary energy function can be used to generate a larger set of grain boundary energies. As an example, the interpolated energies for Σ3 (1429 boundaries), Σ9 (984 boundaries), Σ11 (445 boundaries), and Σ7 (611 boundaries) were compared with the measured grain boundary population in the austenitic steel [12] (see Figs. 9, 10). Nearly continuous sets of boundary energies interpolated from the BRK grain boundary energy function for Σ7 and Σ11 misorientations were linearly correlated with the simulated grain boundary energies. We note that the inverse relationship at each misorientation can be described by the Boltzmann distribution, which is consistent with what has been observed in well-annealed polycrystalline copper [41]. It is therefore possible that this is a common feature of metals with the fcc structure that has evolved by grain growth. Although the numerical parameters in the energy function were obtained only by using the energies of high symmetry boundaries with rotations around <100>, <110>, and <111> axes [32], the strong correlation between the population and energy shows that the BRK energy function is a good predictor for boundaries of all character [58]. The consistency of the simulated energies and experimental observations suggests that it might be possible to create meta-atom (EAM) potentials for other fcc structured complex alloys such as 304, 316, and 316L austenitic steels or even high-entropy alloys and use the BRK grain boundary energy function [32] to calculate the GBEDs. A large data set of interpolated grain boundary energies would be a useful resource for mesoscale simulations of microstructure evolution and can provide an insight into how the grain boundary energies influence the grain boundary population and deformation mechanism in these complex alloys.

Conclusions

The energies of grain boundaries in an austenitic TWIP steel have been simulated using the meta-atom embedded atom method (EAM) potential. The simulated grain boundary energies and the measured grain boundary population in a high-manganese TWIP steel are inversely correlated when groups of boundaries with fixed misorientations are compared. The simulated boundary energies were correlated with the experimental grain boundary energies for the most commonly observed grain boundaries. This is because the uncertainty of the experimentally determined energies decreases as the number of observations increases. We also found that the simulated energies and the energies interpolated from the BRK grain boundary energy function were

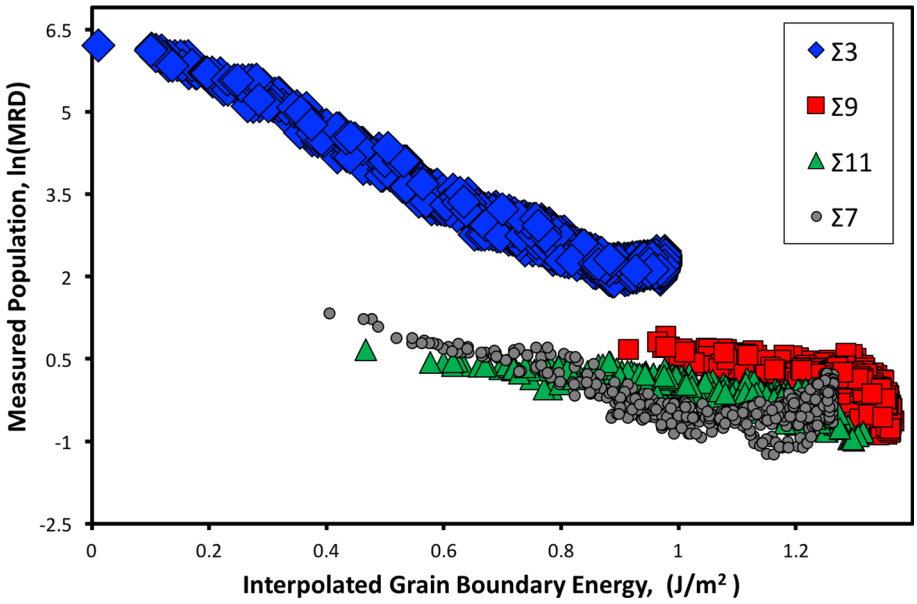

Figure 9 The relationship between grain boundary population [12] and interpolated grain boundary energies derived from the BRK grain boundary energy function [32]. The grain boundaries are divided into four categories Σ3 (blue diamonds), Σ9 (red squares), Σ11 (green triangles), and Σ7 (gray circles).

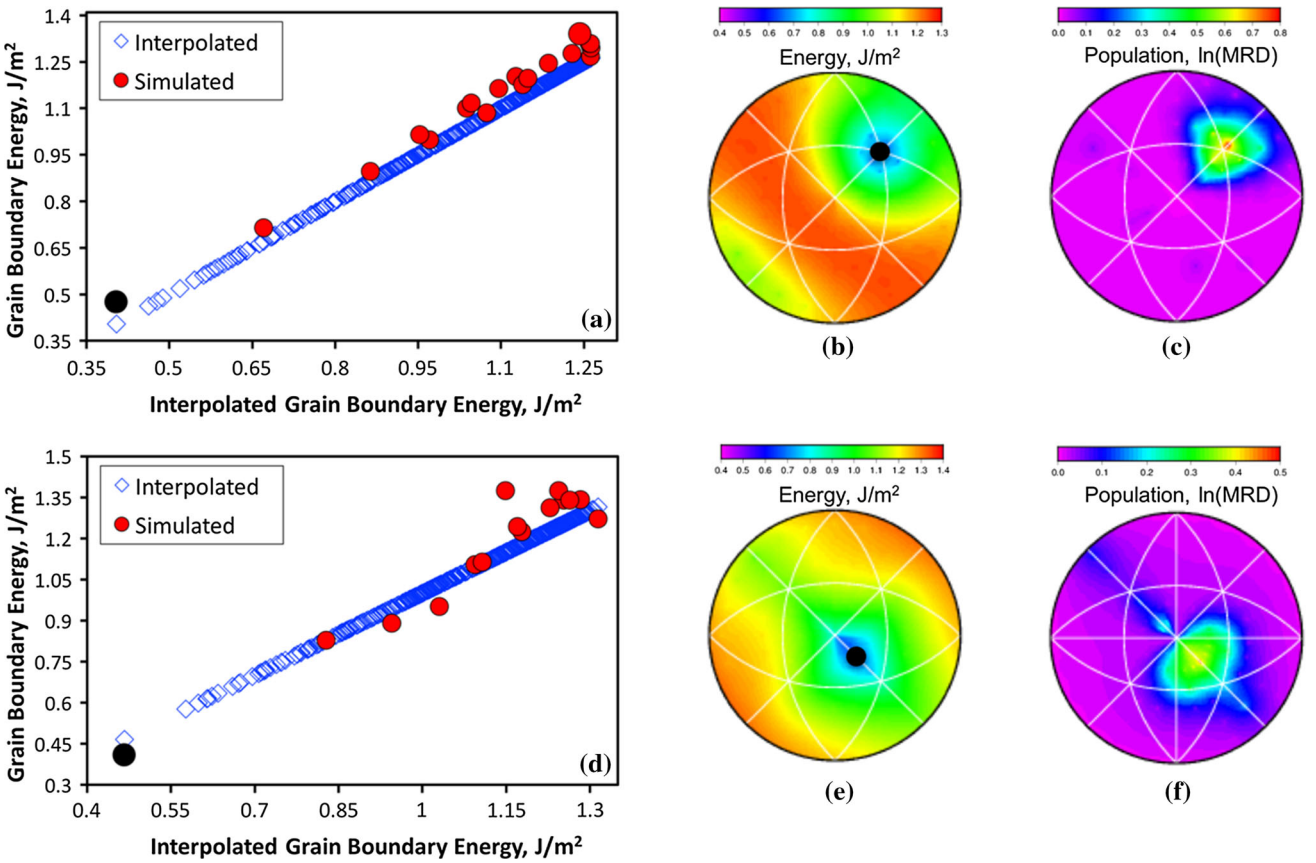

Figure 10 The relationship between the interpolated (blue diamond) and simulated (red circle) grain boundary energies in austenitic steel for Σ7, 38°/[111] (**a**) and Σ11, 51°/[110] (**d**). The distributions of interpolated grain boundary energies and relative grain boundary areas for Σ3 (**b**, **c**) and Σ9 (**e**, **f**) misorientations are plotted on a stereographic projection. The measured grain boundary populations are obtained from Ref. [12]. Noted that the lowest simulated grain boundary energies at the Σ7, 38°/[111] and Σ11, 51°/[110] are marked with black circles.

strongly correlated and also inversely correlated with the measured grain boundary populations. Therefore, grain boundary energies can be reliably estimated from the BRK energy function and this has the potential to foster the microstructural design of austenitic steels and other complex alloys.

Acknowledgements

S.R. acknowledges the financial supports provided by the Skill Development Grant, King Mongkut's University of Technology Thonburi (KMUTT), Research Strengthening Project of the Faculty of Engineering, KMUTT, and the Thailand Research Fund and Office of the Higher Education Commission (MRG6080253). G.S.R. acknowledges support from the National Science Foundation under grant DMR 1628994. The simulating machine supported by the Innovative Software and Computing Center at KMUTT. We also thank Prof. Tawee Tunkasiri and Prof. Poom Kumam for critical comment and suggestion, Dr. David Olmsted for the code used for grain boundary energy calculation, and Dr. Lucas Hale for iprPy calculation framework and the Interatomic Potential Repository Project (NIST).

Electronic supplementary material: The online version of this article (https://doi.org/10.1007/s10853-018-03297-4) contains supplementary material, which is available to authorized users.

References

[1] Bouaziz O, Allain S, Scott CP et al (2011) High manganese austenitic twinning induced plasticity steels: a review of the microstructure properties relationships. Curr Opin Solid State Mater Sci 15:141–168. https://doi.org/10.1016/j.cossms.2011.04.002

[2] Beladi H, Timokhina IB, Estrin Y et al (2011) Orientation dependence of twinning and strain hardening behaviour of a high manganese twinning induced plasticity steel with polycrystalline structure. Acta Mater 59:7787–7799. https://doi.org/10.1016/j.actamat.2011.08.031

[3] Barr CM, Vetterick GA, Unocic KA et al (2014) Anisotropic radiation-induced segregation in 316L austenitic stainless steel with grain boundary character. Acta Mater 67:145–155. https://doi.org/10.1016/j.actamat.2013.11.060

[4] Gutierrez-Urrutia I, Zaefferer S, Raabe D (2010) The effect of grain size and grain orientation on deformation twinning in a Fe–22wt.% Mn–0.6wt.% C TWIP steel. Mater Sci Eng A 527:3552–3560. https://doi.org/10.1016/j.msea.2010.02.041

[5] Michiuchi M, Kokawa H, Wang ZJ et al (2006) Twin-induced grain boundary engineering for 316 austenitic stainless steel. Acta Mater 54:5179–5184. https://doi.org/10.1016/j.actamat.2006.06.030

[6] Shimada M, Kokawa H, Wang ZJ et al (2002) Optimization of grain boundary character distribution for intergranular corrosion resistant 304 stainless steel by twin-induced grain boundary engineering. Acta Mater 50:2331–2341. https://doi.org/10.1016/S1359-6454(02)00064-2

[7] Barr CM, Thomas S, Hart JL et al (2018) Tracking the evolution of intergranular corrosion through twin-related domains in grain boundary networks. NPJ Mater Degrad 2:14. https://doi.org/10.1038/s41529-018-0032-7

[8] Sakaguchi N, Endo M, Watanabe S et al (2013) Radiation-induced segregation and corrosion behavior on Σ3 coincidence site lattice and random grain boundaries in proton-irradiated type-316L austenitic stainless steel. J Nucl Mater 434:65–71. https://doi.org/10.1016/j.jnucmat.2012.11.036

[9] Bouaziz O, Allain S, Scott C (2008) Effect of grain and twin boundaries on the hardening mechanisms of twinning-induced plasticity steels. Scr Mater 58:484–487. https://doi.org/10.1016/j.scriptamat.2007.10.050

[10] Steinmetz DR, Jäpel T, Wietbrock B et al (2013) Revealing the strain-hardening behavior of twinning-induced plasticity steels: theory, simulations, experiments. Acta Mater 61:494–510. https://doi.org/10.1016/j.actamat.2012.09.064

[11] Rohrer GS (2011) Grain boundary energy anisotropy: a review. J Mater Sci 46:5881–5895. https://doi.org/10.1007/s10853-011-5677-3

[12] Beladi H, Nuhfer NT, Rohrer GS (2014) The five-parameter grain boundary character and energy distributions of a fully austenitic high-manganese steel using three dimensional data. Acta Mater 70:281–289. https://doi.org/10.1016/j.actamat.2014.02.038

[13] Jones R, Randle V, Engelberg D, Marrow TJ (2009) Five-parameter grain boundary analysis of a grain boundary–engineered austenitic stainless steel. J Microsc 233:417–422. https://doi.org/10.1111/j.1365-2818.2009.03129.x

[14] Gertsman VY, Bruemmer SM (2001) Study of grain boundary character along intergranular stress corrosion crack paths in austenitic alloys. Acta Mater 49:1589–1598. https://doi.org/10.1016/S1359-6454(01)00064-7

[15] Jones R, Randle V (2010) Sensitisation behaviour of grain boundary engineered austenitic stainless steel. Mater Sci Eng

A 527:4275–4280. https://doi.org/10.1016/j.msea.2010.03.058

[16] Shi F, Tian PC, Jia N et al (2016) Improving intergranular corrosion resistance in a nickel-free and manganese-bearing high-nitrogen austenitic stainless steel through grain boundary character distribution optimization. Corros Sci 107:49–59. https://doi.org/10.1016/j.corsci.2016.02.019

[17] Tokita S, Kokawa H, Sato YS, Fujii HT (2017) In situ EBSD observation of grain boundary character distribution evolution during thermomechanical process used for grain boundary engineering of 304 austenitic stainless steel. Mater Charact 131:31–38. https://doi.org/10.1016/j.matchar.2017.06.032

[18] Feng W, Yang S, Yan Y (2017) Dependence of grain boundary character distribution on the initial grain size of 304 austenitic stainless steel. Philos Mag 97:1057–1070. https://doi.org/10.1080/14786435.2017.1288943

[19] Hu C, Xia S, Li H et al (2011) Improving the intergranular corrosion resistance of 304 stainless steel by grain boundary network control. Corros Sci 53:1880–1886. https://doi.org/10.1016/j.corsci.2011.02.005

[20] Murr LE, Wong GI, Horylev RJ (1973) Measurement of interfacial free energies and associated temperature coefficients in 304 stainless steel. Acta Metall 21:595–604. https://doi.org/10.1016/0001-6160(73)90068-0

[21] Saylor DM, Rohrer GS (2001) Evaluating anisotropic surface energies using the capillarity vector reconstruction method. Interface Sci 9:35–42. https://doi.org/10.1023/A:1011262628243

[22] Holm EA, Olmsted DL, Foiles SM (2010) Comparing grain boundary energies in face-centered cubic metals: Al, Au, Cu and Ni. Scr Mater 63:905–908. https://doi.org/10.1016/j.scriptamat.2010.06.040

[23] Olmsted DL, Foiles SM, Holm EA (2009) Survey of computed grain boundary properties in face-centered cubic metals: I. Grain boundary energy. Acta Mater 57:3694–3703. https://doi.org/10.1016/j.actamat.2009.04.007

[24] Rohrer GS, Holm EA, Rollett AD et al (2010) Comparing calculated and measured grain boundary energies in nickel. Acta Mater 58:5063–5069. https://doi.org/10.1016/j.actamat.2010.05.042

[25] Holm EA, Rohrer GS, Foiles SM et al (2011) Validating computed grain boundary energies in fcc metals using the grain boundary character distribution. Acta Mater 59:5250–5256. https://doi.org/10.1016/j.actamat.2011.05.001

[26] Shibuta Y, Takamoto S, Suzuki T (2008) A molecular dynamics study of the energy and structure of the symmetric tilt boundary of iron. ISIJ Int 48:1582–1591. https://doi.org/10.2355/isijinternational.48.1582

[27] Finnis MW, Sinclair JE (1984) A simple empirical N-body potential for transition metals. Philos Mag A 50:45–55. https://doi.org/10.1080/01418618408244210

[28] Wang P, Xu S, Liu J et al (2017) Atomistic simulation for deforming complex alloys with application toward TWIP steel and associated physical insights. J Mech Phys Solids 98:290–308. https://doi.org/10.1016/j.jmps.2016.09.008

[29] Pierce DT, Jiménez JA, Bentley J et al (2014) The influence of manganese content on the stacking fault and austenite/ε-martensite interfacial energies in Fe–Mn–(Al–Si) steels investigated by experiment and theory. Acta Mater 68:238–253. https://doi.org/10.1016/j.actamat.2014.01.001

[30] Chamati H, Papanicolaou NI, Mishin Y, Papaconstantopoulos DA (2006) Embedded-atom potential for Fe and its application to self-diffusion on Fe(100). Surf Sci 600:1793–1803. https://doi.org/10.1016/j.susc.2006.02.010

[31] Allain S, Chateau J-P, Bouaziz O et al (2004) Correlations between the calculated stacking fault energy and the plasticity mechanisms in Fe–Mn–C alloys. Mater Sci Eng A 387:158–162. https://doi.org/10.1016/j.msea.2004.01.059

[32] Bulatov VV, Reed BW, Kumar M (2014) Grain boundary energy function for fcc metals. Acta Mater 65:161–175. https://doi.org/10.1016/j.actamat.2013.10.057

[33] Ratanaphan S, Olmsted DL, Bulatov VV et al (2015) Grain boundary energies in body-centered cubic metals. Acta Mater 88:346–354. https://doi.org/10.1016/j.actamat.2015.01.069

[34] Ratanaphan S, Boonkird T, Sarochawikasit R et al (2017) Atomistic simulations of grain boundary energies in tungsten. Mater Lett 186:116–118. https://doi.org/10.1016/j.matlet.2016.09.104

[35] Sato K, Ichinose M, Hirotsu Y, Inoue Y (1989) Effects of deformation induced phase transformation and twinning on the mechanical properties of austenitic Fe–Mn–Al alloys. ISIJ Int 29:868–877. https://doi.org/10.2355/isijinternational.29.868

[36] Plimpton SJ (2007) Large-scale atomic/molecular massively parallel simulator. Sandia Natl Lab

[37] Foiles SM (2010) Temperature dependence of grain boundary free energy and elastic constants. Scr Mater 62:231–234. https://doi.org/10.1016/j.scriptamat.2009.11.003

[38] Gupta D (2003) Diffusion, solute segregations and interfacial energies in some material: an overview. Interface Sci 11:7–20. https://doi.org/10.1023/A:1021570503733

[39] Morawiec A, Glowinski K (2013) On "macroscopic" characterization of mixed grain boundaries. Acta Mater 61:5756–5767. https://doi.org/10.1016/j.actamat.2013.06.019

[40] Glowinski K (2014) On identification of symmetric and improperly quasi-symmetric grain boundaries. J Appl

Crystallogr 47:726–731. https://doi.org/10.1107/S160057671400435X

[41] Ratanaphan S, Raabe D, Sarochawikasit R et al (2017) Grain boundary character distribution in electroplated nanotwinned copper. J Mater Sci 52:4070–4085. https://doi.org/10.1007/s10853-016-0670-5

[42] Davison AC, Hinkley DV (1997) Bootstrap methods and their application. Cambridge University Press, Cambridge

[43] Li J, Dillon SJ, Rohrer GS (2009) Relative grain boundary area and energy distributions in nickel. Acta Mater 57:4304–4311. https://doi.org/10.1016/j.actamat.2009.06.004

[44] Saylor DM, Morawiec A, Rohrer GS (2003) The relative free energies of grain boundaries in magnesia as a function of five macroscopic parameters. Acta Mater 51:3675–3686. https://doi.org/10.1016/S1359-6454(03)00182-4

[45] Beladi H, Rohrer GS (2013) The relative grain boundary area and energy distributions in a ferritic steel determined from three-dimensional electron backscatter diffraction maps. Acta Mater 61:1404–1412. https://doi.org/10.1016/j.actamat.2012.11.017

[46] Ratanaphan S, Yoon Y, Rohrer GS (2014) The five parameter grain boundary character distribution of polycrystalline silicon. J Mater Sci 49:4938–4945. https://doi.org/10.1007/s10853-014-8195-2

[47] Gruber J, George DC, Kuprat AP et al (2005) Effect of anisotropic grain boundary properties on grain boundary plane distributions during grain growth. Scr Mater 53:351–355. https://doi.org/10.1016/j.scriptamat.2005.04.004

[48] Beladi H, Rohrer GS (2013) The distribution of grain boundary planes in interstitial free steel. Metall Mater Trans A 44:115–124. https://doi.org/10.1007/s11661-012-1393-0

[49] Ratanaphan S (2013) Grain boundary character distributions in isostructural materials. Ph.D. thesis, Dep Mater Sci Eng Carnegie Mellon Univ

[50] Cantwell PR, Tang M, Dillon SJ et al (2014) Grain boundary complexions. Acta Mater 62:1–48. https://doi.org/10.1016/j.actamat.2013.07.037

[51] Raabe D, Herbig M, Sandlöbes S et al (2014) Grain boundary segregation engineering in metallic alloys: a pathway to the design of interfaces. Curr Opin Solid State Mater Sci 18:253–261. https://doi.org/10.1016/j.cossms.2014.06.002

[52] Kuzmina M, Ponge D, Raabe D (2015) Grain boundary segregation engineering and austenite reversion turn embrittlement into toughness: example of a 9 wt.% medium Mn steel. Acta Mater 86:182–192. https://doi.org/10.1016/j.actamat.2014.12.021

[53] Deng Y, Tasan CC, Pradeep KG et al (2015) Design of a twinning-induced plasticity high entropy alloy. Acta Mater 94:124–133. https://doi.org/10.1016/j.actamat.2015.04.014

[54] Frolov T, Olmsted DL, Asta M, Mishin Y (2013) Structural phase transformations in metallic grain boundaries. Nat Commun 4:1899. https://doi.org/10.1038/ncomms2919

[55] Frolov T, Asta M, Mishin Y (2015) Segregation-induced phase transformations in grain boundaries. Phys Rev B 92:020103. https://doi.org/10.1103/PhysRevB.92.020103

[56] Kurtuldu G, Sicco A, Rappaz M (2014) Icosahedral quasicrystal-enhanced nucleation of the fcc phase in liquid gold alloys. Acta Mater 70:240–248. https://doi.org/10.1016/j.actamat.2014.02.037

[57] Thomas SL, Chen K, Han J et al (2017) Reconciling grain growth and shear-coupled grain boundary migration. Nat Commun 8:1764. https://doi.org/10.1038/s41467-017-01889-3

[58] Homer ER, Patala S, Priedeman JL (2015) Grain boundary plane orientation fundamental zones and structure-property relationships. Sci Rep 5:15476. https://doi.org/10.1038/srep15476